Research Square

Preprints are preliminary reports that have not undergone peer review.
They should not be considered conclusive, used to inform clinical practice,
or referenced by the media as validated information.

Time-varying mesh stiffness for fast force estimation on cracked and healthy double helical gears

Sophie-Maria Rauscher

sophie-maria.rauscher@dlr.de

Deutsches Zentrum für Luft- und Raumfahrt e. V. (DLR)

Aryan Thosar

Deutsches Zentrum für Luft- und Raumfahrt e. V. (DLR)

Behara Neha

Research Article

Keywords:

Posted Date: November 13th, 2026

DOI: https://doi.org/10.21203/rs.3.rs-11366043/v1

License: This work is licensed under a Creative Commons Attribution 4.0 International License.
Read Full License

Additional Declarations: No competing interests reported.

Time-varying mesh stiffness for fast force estimation on cracked and healthy double helical gears

Sophie-Maria Rauscher[1*], Aryan Thosar[1†] and Behara Neha[1†]

[1*]Institute for Test and Simulation of Gas Turbines , DLR, Forschungsallee 1, Augsburg, 86159, Bavaria, Germany.

*Corresponding author(s). E-mail(s): sophie-maria.rauscher@dlr.de;
†These authors contributed equally to this work.

Abstract

Time-Varying-Mesh-Stiffness (TVMS) in the context of gearing has traditionally been studied from a theoretical standpoint. This work strives to summarize in a concise manner notable literature pertaining to TVMS and proposes a methodology to extend its utility to the computation of time-dependent forces on gear flanks. This is done by calculating the share of individual tooth stiffnesses to the total mesh stiffness at any given instant of time, and relating this fraction to the instantaneous distribution of forces amongst the teeth in the mesh, under the assumption of parallel spring configuration. In this paper, the effects of the introduction of a crack in the tooth root is also investigated.

Gearbox vibrations and premature tooth failure are often accompanied by time-varying internal loading that occurs during the mesh-in and mesh-out phases of gear-tooth contact. Direct finite-element analysis of these forces is computationally prohibitive, motivating the development of an analytical framework based on time-varying mesh stiffness (TVMS). This work presents a comprehensive TVMS model for double-helical gear pairs that accommodates both healthy and surface-cracked teeth. Leveraging a slice-wise decomposition of the gear tooth—where each infinitesimal spur-slice contributes a series of bending, shear, axial, fillet, and Hertzian compliances—the model yields closed-form expressions for the stiffness of individual slices and aggregates them to obtain the total mesh stiffness as a function of roll angle. An explicit algorithm guides the workflow from geometry definition through force computation, including the treatment of crack geometry (straight-line and parabolic limiting lines) and its influence on cross-sectional area and moment of inertia.

The results demonstrate that the TVMS framework provides a rapid, physics-based alternative to full FEM analyses for evaluating gear-tooth forces, assessing the impact of defects, and supporting dynamic-response studies of high-speed helical and double-helical gear trains. Future work will focus on experimental validation and extension to multiple or more complex cracks.

Keywords: TVMS, non-straight toothing, time-dependent forces, cracked root, non-comparability

1 Introduction

Gearbox vibrations not only produce a noisy powertrain operation but also raise the risk of premature gear failure, with fatigue being a primary underlying cause [1]. The excitation sources are multifactorial: assembly errors, manufacturing defects, and external cyclic forces. Even though many of these are post-design issues, the time-varying forces acting on a gear tooth flank during the mesh-in and mesh-out processes must be understood quantitatively because this internal cyclic loading drastically reduces the expected cycle life.

Estimating gear-tooth forces directly from a finite-element analysis (FEA) is expensive in both time and computational resources. Instead, a predictive model based on time-varying mesh stiffness (TVMS) can be used to estimate these forces a priori, thus making a subsequent FEA/MBD (multi-body dynamics) analysis of deflections far more efficient. TVMS describes how the mesh stiffness of a gear pair varies with the contact angle, and it can be correlated with the force distribution among the meshing teeth.

This paper develops a TVMS framework specifically for helical and double-helical gear systems. It incorporates both healthy and cracked gear teeth, providing a comprehensive load-sharing description. A step-by-step algorithm guides the reader through the workflow, from geometry definition to force computation. Finally, the numerical results are benchmarked against the literature, and the theoretical implications are summarised in the concluding section.

Ma *et al.* [2] derived an expression for the total potential energy stored in a deflected spur-gear tooth using beam theory. The energy was decomposed into five components (transverse shear, bending, compression, fillet foundation, and Hertzian contact). The inverse stiffness counterparts were then derived, revealing that the components behave like a series of springs. They also investigated how cracks of different geometries affect the TVMS of spur-gear systems. Cao *et al.* [3] presented analytical expressions for deflections under bending, shear, and compressive loads, and related them to the corresponding stiffnesses. Their results were compared with the "No-Load-Transmission-Error Dynamics" formulation, which incorporates static stiffness into the equations of motion to predict time-dependent forces. Feng *et al.* [4] treated a helical-gear face as a parallel combination of infinitesimally thin spur slices. Summation of the slice stiffness contributions yielded a compact overall stiffness expression that can handle varying numbers of slices in contact. Velex *et al.* [5] modelled local properties (stiffness, contact-line length) as periodic functions. By expanding them in a Fourier series they extracted an *average stiffness* compliant with ISO 6336 and a *time-varying component* that captures the short-term fluctuations.Liu *et al.* [6] related contact ratios, contact-line length, and mesh stiffness of helical pairs. Choe *et al.* [7] expanded this to the engagement process, deriving start-and-end mesh angles and hence the total mesh duration for a tooth pair. Yang *et al.* [1] extended the models from spur/helix to double-helix gears, highlighting the importance of groove width and the emergence of additional axial stiffness components in the double-helix

geometry.

Mesh-stiffness modelling is essential for gear design and analysis, as it determines how gears resist deformation and transmit loads efficiently [8, 9]. Factors such as gear geometry, material properties, tooth profile, contact pattern, and lubrication are all encapsulated in mesh-stiffness models to predict contact stresses and power losses. Accurate representations lay the foundation for dynamic analyses of high-speed spur-gear systems [8, 9].

The nonlinear frequency-response characteristics of gear pairs have been extensively studied with an emphasis on incorporating accurate TVMS. Yang *et al.* [10] showed that precise predictions of system responses hinge on a correct TVMS implementation. Their stability analysis highlighted the boundary between stable and unstable operating regimes. Jiang *et al.* [11] studied parameter-excited oscillations in multi-mesh systems, revealing that the phasedifference between mesh-stiffness variations at two meshes can trigger severe vibrations. Chang *et al.* [12] proposed a hybrid finite-element-method (FEM)/elastic-contact model that accurately predicted TVMS and load distribution while being computationally efficient. Kahraman *et al.* [13] incorporated bearing compliance and torsion–transverse coupling into a geared-rotor model, while Chen *et al.* [14] examined ring flexibility in planetary gears, revealing significant periodic variations in mesh stiffness.

The severity of gear cracks is commonly assessed by the reduction in mesh stiffness they cause [15]. Numerous studies have investigated crack propagation effects using both analytical and numerical methods: The influence of gear cracks on mesh stiffness has been examined by many researchers. Tian *et al.* [16] carried out a purely analytical study of how dynamic crack effects modify the mesh stiffness, while Wu *et al.* [17] employed finite-element analysis to show how varying crack sizes alter gearbox dynamics. Yousfi *et al.* [18] introduced a double-discretisation approach based on potential-energy theory for spur gears with surface defects. Pandya *et al.* [19] simulated crack propagation in a single tooth of a spur gear using a linear-elastic-fracture-mechanics (LEFM)–based FE program and quantified the resulting percentage reduction in total mesh stiffness. Zhou *et al.* [20] developed a 16-degree-of-freedom model to investigate the vibration response of different crack levels, employing signal-processing techniques for crack detection. Shao *et al.* [21] coupled a dynamic model with a 3-D FEM to investigate natural frequencies and vibration shapes in cracked gear systems. Yu *et al.* [22] examined the influence of spatial crack propagation on time-varying mesh stiffness (TVMS) and load-sharing ratios for involute spur-gear sets, assuming a quasi-parabolic crack path. Jiang *et al.* [23] presented analytical mesh-stiffness models that incorporate gear-body deflection for a cracked tooth and its adjacent tooth; these models were validated with a dynamic simulation with 6 degrees of freedom. Zouari *et al.* [24] captured the instantaneous alteration in mesh stiffness at the base of a cracked tooth, demonstrating how crack depth modulates gear flexibility. Liang *et al.* [25] investigated the impact of cracks on a planetary

transmission system through mesh-stiffness evolution and vibration-signature identification. Saxena *et al.* [26] reported a consistent decrease in natural frequencies as crack size increased, indicating that specific modes could serve as crack-fault indicators. Lewicki *et al.* [27] and Zouari *et al.* [28] used LEFM and FEA to estimate mode-I stress-intensity factors, thereby predicting crack-propagation life in gear rim experiments. Chen *et al.* [29, 30] examined crack growth along both tooth width and depth, employing root mean square statistical indicators and frequency-spectrum analysis to validate FEM results. Finally, Yang *et al.* [1] focused on calculating TVMS while considering transmission-ratio effects for cracked gears.

2 Theoretical Background

The stiffness of a gear mesh is a cornerstone of any dynamic or structural analysis of a gear train. It governs how effectively the mesh can transmit loads, how the system responds to excitation, and consequently how noise, vibration, and fatigue behaviour evolve. Mesh-stiffness modelling therefore incorporates a multitude of mechanical, geometric, and material factors: gear geometry, tooth profile, contact pattern, lubrication regime, and the mechanical properties of the constituent material. The overall stiffness of a gear tooth can be regarded as the sum of several contributions, each arising from a distinct deformation mechanism. Feng *et al.* [4] and Wu *et al.* [31] have shown that the total compliance of a tooth can be decomposed into axial, transverse, and contact-related components. In the following, we employ the analytical framework developed by Yang *et al.* [32] and Wang *et al.* [33] for double-helical gears and extend it by incorporating axial contributions that are specific to the double-helix geometry.

A double-helical gear is characterized by two helices of opposite sense, separated by a central groove. The effective face width is therefore

$$W_{\text{total}} = 2\,W + W_{\text{groove}}, \tag{1}$$

where W is the face width of a single helix and W_{groove} is the groove width.

where W denotes the face width of one helix and W_{groove} is the width of the groove. For a helical tooth we consider a "slice" model: the tooth is represented as a stack of infinitesimally thin spur-gear sections distributed along the face-width direction. Each slice has a thickness dW and experiences shear, bending, or compression. The area of a single slice and its moment of inertia about the neutral axis are

$$A_x = 2\,y\,dW \tag{2}$$

$$I_x = \frac{2}{3}\,y^{\,3}\,dW. \tag{3}$$

respectively (cf. figure 1). The axial direction is x, the transverse direction y.

The tooth surface is divided into two distinct zones: a transition profile (from the root to the involute start) and a pure involute profile (from the involute start to the addendum). For any point on the transition segment $(A{-}C)$ the Cartesian coordinates are

$$x_\gamma = R_p\,\cos\beta - \left(\frac{A}{\sin\gamma} + R_\gamma\right)\,\sin(\gamma-\beta), \tag{4}$$

$$y_\gamma = R_p\,\sin\beta - \left(\frac{A}{\sin\gamma} - R_\gamma\right)\,\cos(\gamma-\beta), \tag{5}$$

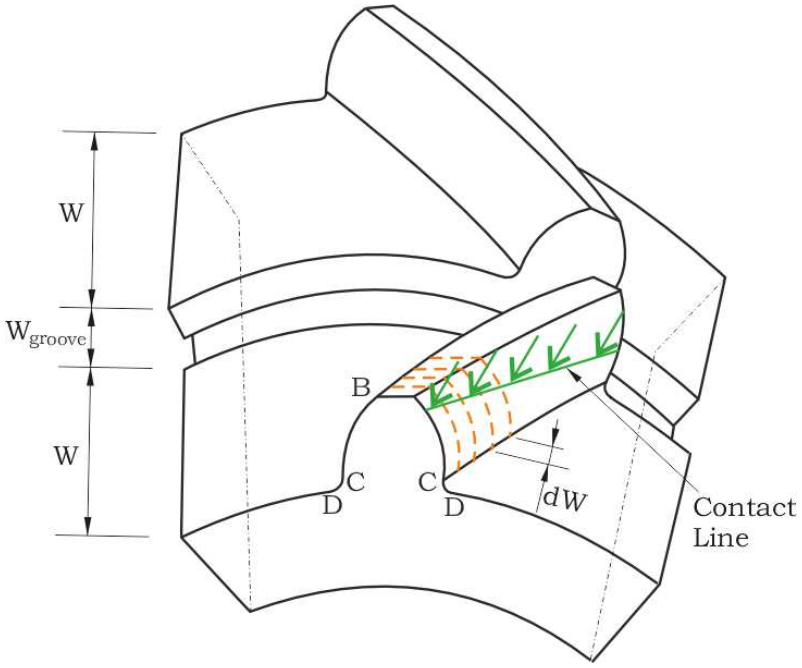


Fig. 1: Description of parameters at double-helical gear

where R_p is the pitch radius, R_γ the radius at angle γ, and β the helix angle. In the involute region $(C-D)$ the standard involute parametric equations apply:

$$x_\tau = R_b \Big[(\tau + \theta_{\text{half}}) \, \sin\tau + \cos\tau \Big], \tag{6}$$

$$y_\tau = R_b \Big[(\tau + \theta_{\text{half}}) \, \cos\tau - \sin\tau \Big]. \tag{7}$$

with R_b the base radius and θ_{half} is given in Luo *et al.* [34].

The overall stiffness of a double-helical tooth can be decomposed into eight distinct compliance terms:

1. transverse bending stiffness, k_{tb},

$$\begin{aligned} \frac{1}{k_{tb}} = &\int_{\frac{\pi}{2}}^{\alpha_t} \frac{((x_P - x_\gamma)\,\cos(\alpha_P) - y_P \sin(\alpha_P))^2 \cos^2(\beta)}{EI_{x_\gamma}} \frac{\mathrm{d}x_\gamma}{\mathrm{d}\gamma}\,\mathrm{d}\gamma \\ &+ \int_{\alpha_c}^{\alpha_P} \frac{((x_P - x_\tau)\,\cos(\alpha_P) - y_P\,\sin(\alpha_P))^2 \cos^2(\beta)}{EI_{x_\tau}} \frac{\mathrm{d}x_\tau}{\mathrm{d}\tau}\,\mathrm{d}\tau, \end{aligned} \tag{8}$$

2. transverse shear stiffness, k_{ts},

$$\begin{aligned}\frac{1}{k_{ts}} = &\int_{\frac{\pi}{2}}^{\alpha_t} \frac{1.2\,\cos^2(\alpha_P)\,\cos^2(\beta)}{GA_{x_\gamma}}\,\frac{\mathrm{d}x_\gamma}{\mathrm{d}\gamma}\,\mathrm{d}\gamma \\ &+\int_{\alpha_c}^{\alpha_P} \frac{1.2\,\cos^2(\alpha_P)\cos^2(\beta)}{GA_{x_\tau}}\frac{\mathrm{d}x_\tau}{\mathrm{d}\tau}\,\mathrm{d}\tau,\end{aligned} \tag{9}$$

3. transverse compression stiffness, k_{ta},

$$\begin{aligned}\frac{1}{k_{ta}} = &\int_{\frac{\pi}{2}}^{\alpha_t} \frac{\sin^2(\alpha_P)\,\cos^2(\beta)}{EA_{x_\gamma}}\,\frac{\mathrm{d}x_\gamma}{\mathrm{d}\gamma}\,\mathrm{d}\gamma \\ &+\int_{\alpha_c}^{\alpha_P} \frac{\sin^2(\alpha_P)\,\cos^2(\beta)}{EA_{x_\tau}}\,\frac{\mathrm{d}x_\tau}{\mathrm{d}\tau}\,\mathrm{d}\tau\,.\end{aligned} \tag{10}$$

4. transverse contribution of the root-fillet radius, k_{tf},

$$\frac{1}{k_{tf}} = \frac{\cos^2(\alpha_P)\,\cos^2(\beta)\,(L^*(\frac{u_f}{S_f})^2 + M^*\,\frac{u_f}{S_f} + P^*(1 + Q^*\,\tan^2(\alpha_t)))}{E \cdot dW} \tag{11}$$

5. axial bending stiffness (specific to a double-helical configuration), k_{ab},

$$\begin{aligned}\frac{1}{k_{ab}} = &\int_{\frac{\pi}{2}}^{\alpha_t} \frac{3\,\sin^2(\beta)\,(x_P - x_\gamma)^2}{E\,dW^3\,y_\gamma}\,\frac{dx_\gamma}{d\gamma}\,d\gamma \\ &+\int_{\alpha_c}^{\alpha_P} \frac{3\,\sin^2(\beta)\,(x_P - x_\tau)^2}{E\,dW^3\,y_\tau}\,\frac{dx_\tau}{d\tau}\,d\tau,\end{aligned} \tag{12}$$

6. axial torsion stiffness (specific to a double-helical configuration), k_{at},

$$\begin{aligned}\frac{1}{k_{at}} = &\int_{\frac{\pi}{2}}^{\alpha_t} \frac{3\,\sin^2(\beta)\,\cos^2\beta\,y_P^2}{G\,(4\,dW\,y_\gamma^3 + dW^3\,y_\gamma)}\,\frac{dx_\gamma}{d\gamma}\,d\gamma \\ &+\int_{\alpha_c}^{\alpha_P} \frac{3\,\sin^2(\beta)\,\cos^2\beta\,y_P^2}{G\,(4\,dW\,y_\tau^3 + dW^3\,y_\tau)}\,\frac{dx_\tau}{d\tau}\,d\tau,\end{aligned} \tag{13}$$

7. axial contribution of the root-fillet radius (specific to a double-helical configuration), k_{af},

$$\frac{1}{k_{af}} = \int_0^{R_r} \frac{\sin^2(\beta)\,(x_P - x)^2}{E\,I_{af}}\,dx, \tag{14}$$

8. non-linear (Hertzian) contact stiffness at the tooth-to-tooth contact, k_h

$$\frac{1}{k_h} = \frac{4\,(1-\nu^2)}{\pi\,E \cdot dW}. \tag{15}$$

For brevity we denote α_t the transverse pressure angle, α_c the pressure angle in the starting point of involute curve, α_P the pressure angle at the point of contact, E Young's modulus, G the shear modulus, and S_f the tooth thickness. The parameters L^*, M^*, P^*, Q^*, u_f are taken from Sainsot *et al.* [35].

The axial second-moment of area I_{af} of the fillet section is a piecewise function:

$$I_{af} = \begin{cases} \dfrac{W^3\left(\sqrt{R_r^2 - x^2} - \sqrt{R_h^2 - x^2}\right)}{3} + \\ \dfrac{\left(\frac{W_{\text{groove}}}{2}\right)^3\left(\sqrt{R_r^2 - x^2} - \sqrt{R_h^2 - x^2}\right)}{3}, & R_h \geq x \geq 0 \\ \dfrac{W^3\sqrt{R_r^2 - x^2} + \left(\frac{W_{\text{groove}}}{2}\right)^3\sqrt{R_g^2 - x^2}}{3}, & R_g \geq x \geq R_h \\ \dfrac{W^3\sqrt{R_r^2 - x^2}}{3}, & R_r \geq x \geq R_g \end{cases} \tag{16}$$

where R_r, R_h, and R_g are the root, hub, and groove radii, respectively.

For a pair of slices belonging to the pinion (p) and the gear (g), the overall compliance is the sum of all constituent compliances:

$$\begin{aligned} \frac{1}{k_{\text{single slice}}} = &\frac{1}{k_{ta_p}} + \frac{1}{k_{tb_p}} + \frac{1}{k_{ts_p}} + \frac{1}{k_{tf_p}} + \frac{1}{k_{ab_p}} + \frac{1}{k_{at_p}} + \frac{1}{k_{af_p}} \\ &+ \frac{1}{k_{ta_g}} + \frac{1}{k_{tb_g}} + \frac{1}{k_{ts_g}} + \frac{1}{k_{tf_g}} + \frac{1}{k_{ab_g}} + \frac{1}{k_{at_g}} + \frac{1}{k_{af_g}} + \frac{1}{k_h} \end{aligned} \tag{17}$$

where the subscript h refers to the Hertzian contact common to both gears.

Let the face width be divided into N slices of equal thickness dW. For a given roll angle θ the number of active slices in contact is $N(\theta)$. The stiffness of a single tooth pair is the sum of the slice-pair compliances:

$$k_{\text{single, pair}} = \sum_{j=1}^{N(\theta)} k_{\text{slice},\, j}, \tag{18}$$

where $k_{\text{slice},j}$ is given by Eq. (17). When n such tooth pairs are simultaneously in contact at the same roll angle, the total mesh stiffness is

$$k_{\text{total},\,\theta} = \sum_{q=1}^{n} k_{\text{single,pair},\,q}. \tag{19}$$

Equations (18) and (19) therefore yield the overall mesh stiffness of a double-helical gear for any prescribed roll angle, provided the slice thickness dW and the number of contact pairs are known.

Analytical description of cracks in tooth root

Cracks in gear teeth reduce the load-bearing area, thereby lowering the stiffness of the affected tooth and limiting the overall load-carrying capacity. Consequently, the share of the meshing load is redistributed to the remaining healthy teeth, which may then experience higher than nominal stresses. This redistribution makes the healthy teeth vulnerable to crack initiation, pitting and a variety of other failure mechanisms. A detailed study of crack growth in gear teeth is therefore essential.

In this work we focus exclusively on cracks that originate at the tooth root and propagate in the transverse direction (figure 2). Cracks that advance along the tooth axis are outside the scope of the present report. Ma *et al.* [2] carried out a comprehensive analysis of this crack family, and the model we adopt here is a direct excerpt from their paper.

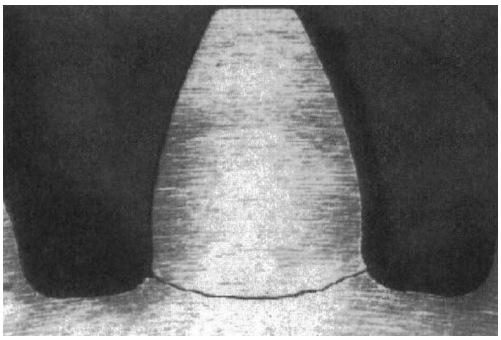


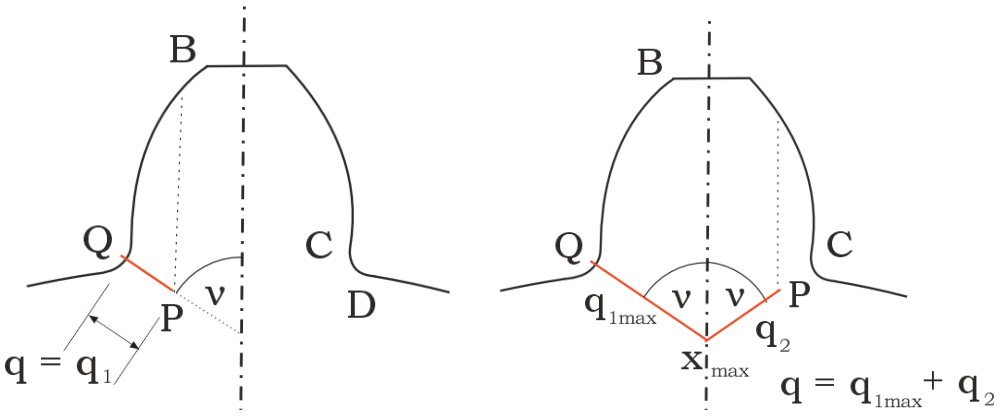
Fig. 2: Crack in tooth root and propagated in transverse direction under study [2]

The mere presence of a crack can be reduced to a change in the cross-sectional area that resists the induced stresses and the corresponding area moments of inertia — an effect that is independent of the specific gear type. Ma *et al.* [2] propose three distinct models for the geometry under investigation, based on the "limiting line" that connects the crack tip to the tooth tip. Two crack shapes (straight line and parabolic curve) and two limiting lines (straight and parabolic) are considered in the paper; the following text reproduces those cases.

Case 1: Straight line crack path with a straight limiting line

Figure 3 illustrates a crack that originates at the tooth root and propagates as a straight line toward the tooth tip. Measured from the tooth root to the crack tip, the crack depth is denoted q_1; the maximum depth, $q_{1\,\max}$, is attained when the tip reaches the tooth central axis. Consequently, the tip location can be specified by the Cartesian pair $(x_p,\, y_p)$. Together with the propagation angle ν (measured from the radial direction), completes the geometric description of the crack.

In order to find the tip coordinates (x_p, y_p), the coordinates of the initiation point Q are required. Once (x_q, y_q) are known, the tip coordinates follow from the simple trigonometric relations



(a) Crack tip above the tooth central axis (b) Crack tip below the tooth central axis

Fig. 3: Straight line crack path with a straight limiting line

$$x_p = x_q - q_1 \cos\nu, \tag{20}$$
$$y_p = y_q - q_1 \sin\nu. \tag{21}$$

The y–coordinate of the projection point G on the involute curve is simply $y_g = y_p$. To obtain x_g one solves equation (6) for the involute angle τ.

Because the crack tip may lie either above or below the tooth central axis, the cross-sectional area and its moment of inertia must be treated in two separate sub-cases.

Condition a: Crack tip above the tooth central axis

$$I_x = \begin{cases} \dfrac{(y_q + y)^3\, W}{12} & \text{for } x_p \le x \le x_g, \\ \dfrac{2\, y^3\, W}{3} & \text{otherwise,} \end{cases} \tag{22}$$

$$A_x = \begin{cases} (y_q + y)\, W & \text{for } x_p \le x \le x_g, \\ 2\, y\, W & \text{otherwise.} \end{cases} \tag{23}$$

Condition b: Crack tip below the tooth central axis

$$I_x = \begin{cases} \dfrac{2\, y^3\, W}{3} & x < x_{\max}, \\ \left(y - \frac{(x - x_{\max})\, y_q}{x_p - x_{\max}}\right)^3 \dfrac{W}{12} & x_{\max} \le x < x_p, \\ (y - y_q)^3\, \dfrac{W}{12} & x_p \le x \le x_g, \\ 0 & \text{otherwise.} \end{cases} \tag{24}$$

$$A_x = \begin{cases} 2\,y\,W & x < x_{\max}, \\ \left(y - \frac{(x - x_{\max})\,y_q}{x_p - x_{\max}}\right) W & x_{\max} \le x < x_p, \\ (y - y_q)\,W & x_p \le x \le x_g, \\ 0 & \text{otherwise.} \end{cases} \tag{25}$$

Case 2: Straight line crack path with a parabolic limiting line

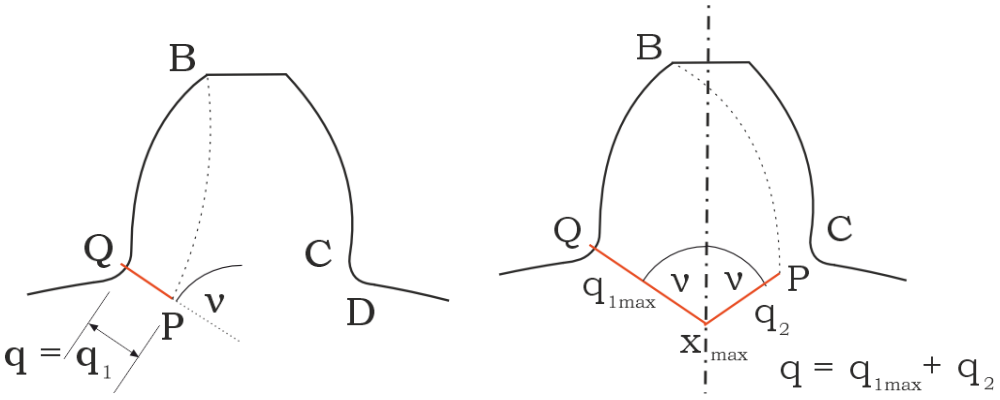
Figure 4 shows the second crack configuration: a straight crack path that follows a parabolic limiting line. Sticking to the same nomenclature as in case 1, additional the coordinates of the "bottom" (or apex) of the parabolic limiting line (the point where the limiting line meets the tooth root) $(x_b,\, y_b)$ are needed. Also the projection of the crack tip onto the involute curve $(x_g,\, y_g)$ (cf. figure 4) is used.

The tip coordinates (x_p, y_p) are obtained exactly as in case 1 (equation (20) – (21)); only the limiting line now follows the parabola

$$y(x) = y_p + \frac{y_b - y_p}{(x_b - x_p)^2}\,(x - x_p)^2\,, \tag{26}$$

which is used in the expressions for the section area and its moment of inertia.

Because the crack tip may again lie either above or below the tooth central axis, we distinguish two sub-cases.



(a) Crack tip above the tooth central axis (b) Crack tip below the tooth central axis

Fig. 4: Straight line crack path with a parabolic limiting line

Condition a: Crack tip above the tooth central axis

$$I_x = \begin{cases} \frac{2\,y^3\,W}{3} & x \le x_p \\ (\frac{(y_b - y_p)\cdot(x-x_p)^2}{(x_b-x_p)^2} + y_p + y)^3\,\frac{W}{12} & otherwise \end{cases} \tag{27}$$

$$A_x = \begin{cases} 2\,y\,W & x \le x_p \\ \left(\frac{(y_b - y_p)\cdot(x-x_p)^2}{(x_b-x_p)^2} + y_p + y\right)\,W & otherwise \end{cases} \tag{28}$$

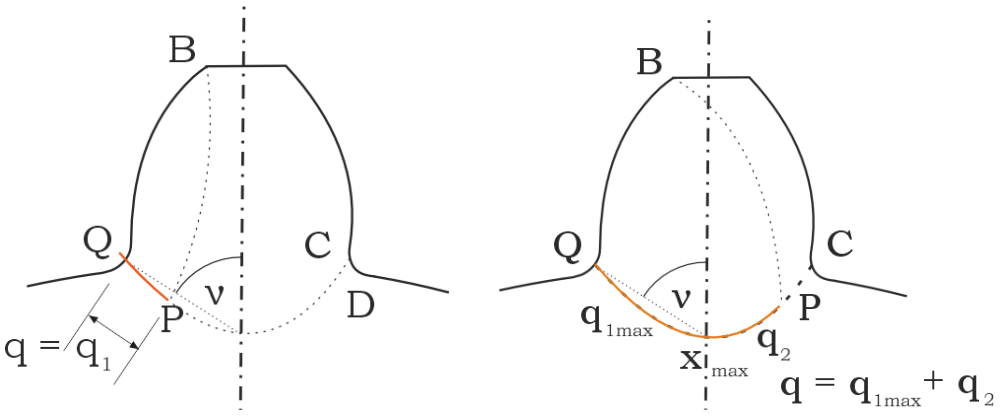
Condition b: Crack tip below the tooth central axis

$$I_x = \begin{cases} \frac{2\,y^3\,W}{3} & x \le x_{max} \\ (y - \frac{(x-x_{max})\,y_p}{x_p - x_{max}})^3\,\frac{W}{12} & x_{max} < x \le x_p \\ (\frac{(y_b + y_p)\cdot(x-x_p)^2}{(x_b-x_p)^2} - y_p + y)^3\,\frac{W}{12} & otherwise \end{cases} \tag{29}$$

$$A_x = \begin{cases} 2\,y\,W & x \le x_p \\ (y - \frac{(x-x_{max})\,y_p}{x_p - x_{max}})\,W & x_{max} < x \le x_p \\ (\frac{(y_b + y_p)\cdot(x-x_p)^2}{(x_b-x_p)^2} - y_p + y)\,W & otherwise \end{cases} \tag{30}$$

Case 3: Parabolic line crack path with a parabolic limiting line

Figure 5 shows the third crack configuration: a parabolic crack path bounded by a parabolic limiting line. For the case in which the crack tip is still "above" the tooth central axis the geometry and the corresponding sectional properties are identical to those of case 2; the moment of inertia and the cross-sectional area are therefore given again by equations (27) and (28).



(a) Crack tip above the tooth central axis (b) Crack tip below the tooth central axis

Fig. 5: Parabolic line crack path with a parabolic limiting line

When the crack tip has "traversed" the tooth central axis (a scenario depicted in figure 5), the section below the axis no longer follows the straight-line expression of

case 1 but must take into account the parabolic geometry of the limiting line. The resulting expressions for the section moment of inertia and the cross-sectional area are

$$I_x = \begin{cases} \dfrac{2\,y^3\,W}{3} & x \le x_{\max}, \\ \left(y - \sqrt{\dfrac{(x - x_{\max})\,y_q^2}{x_q - x_{\max}}}\right)^3 \dfrac{W}{12} & x_{\max} < x \le x_p, \\ \left(\frac{(y_b+y_p)(x-x_p)^2}{(x_b-x_p)^2} - y_p + y\right)^3 \dfrac{W}{12} & \text{otherwise.} \end{cases} \tag{31}$$

$$A_x = \begin{cases} 2\,y\,W & x \le x_p, \\ \left(y - \sqrt{\dfrac{(x - x_{\max})\,y_q^2}{x_q - x_{\max}}}\right) W & x_{\max} < x \le x_p, \\ \left(\frac{(y_b+y_p)(x-x_p)^2}{(x_b-x_p)^2} - y_p + y\right) W & \text{otherwise.} \end{cases} \tag{32}$$

All in all, the third model is the most realistic one because it represents the true parabolic crack-propagation behaviour. Nevertheless, a comparison of the axial stiffnesses obtained from the three suggested models shows only a negligible difference (typically $< 1\%$); hence, for simplicity and to keep the subsequent analysis transparent, case 1 (i.e. the straight-line case) can be used for all remaining calculations.

Estimation of normal forces and load redistribution

With the TVMS framework for inclined-tooth gears in hand, we can now estimate the instantaneous normal forces on individual tooth pairs, both for cracked and for uncracked gears. These forces are required as inputs for FEM, vibration, or dynamic-analysis studies and ultimately inform better design decisions.

For a multi-tooth pair contact (a total of n_{healthy} healthy pairs), the overall mesh stiffness is the result of a parallel combination of the stiffnesses of each pair in mesh:

$$k_{\text{total}} \;=\; \sum_{j=1}^{n_{\text{healthy}}} k_{j,\theta}\,. \tag{33}$$

If the total normal load acting on all teeth in simultaneous mesh is F_N, then the normal force transmitted by pair i at roll angle θ follows directly from the stiffness proportion

$$F_{N,i,\theta} \;=\; F_N\,\frac{k_{i,\theta}}{k_{\text{total}}}\,. \tag{34}$$

For a helical gear transmitting a torque T the tangential force is

$$F_{\tan} \;=\; \frac{T}{R_p}\,. \tag{35}$$

The corresponding radial and axial components are

$$F_{rad} = F_{\tan}\,\tan(\alpha_t), \tag{36}$$

$$F_{ax} = F_{\tan}\,\tan(\beta). \tag{37}$$

The overall normal force on a healthy tooth pair is therefore

$$F_N \;=\; \sqrt{F_{\tan}^2 + F_{rad}^2 + F_{ax}^2}\,. \tag{38}$$

For healthy double-helical gears the load is equally shared between the two sides. Consequently the normal force on a single side is

$$F_N^{(\text{side})} \;=\; \frac{1}{2}\,F_N\,. \tag{39}$$

If a crack appears on one side, the stiffness of that side changes (k_{cracked}). The normal forces then redistribute according to a simple proportionality law

$$F_N^{(\text{cracked})} = F_N\,\frac{k_{\text{cracked}}}{k_{\text{cracked}} + k_{\text{healthy}}}\,, \tag{40}$$

$$F_N^{(\text{healthy})} = F_N\,\frac{k_{\text{healthy}}}{k_{\text{cracked}} + k_{\text{healthy}}}\,. \tag{41}$$

If a crack appears on a particular meshing tooth, the force on that particular pair i follows the same proportionality as Eqs. (34):

$$F_{N,i,\theta} \;=\; F_{\text{side}}\,\frac{k_{i,\theta}}{k_{\text{total}}}\;, \tag{42}$$

with the understanding that $k_{i,\theta}$ is now the reduced stiffness of the cracked pair.

Finally, when a cracked tooth meshes with an uncracked tooth, the forces on the two mating teeth remain equal and in dynamic equilibrium. Thus, the above redistribution formulas (Eqs. (40) and (41)) still apply to both sides, ensuring that the net moment and normal force balance are preserved.

Analysis of contact-line regimes and mesh stiffness evolution

Depending on the contact-line inclination β_b, the transverse travel (or, more precisely, the mesh period) and the face-width W, three distinct regimes can be distinguished by Choe *et al.* [7].

Intuitively, when the transverse travel exceeds the face-width, the longest contact line covers the *entire* face-width for a finite interval of the roll angle (case 1). Conversely, when the travel is higher than the face-width, only a fraction of the face-width is engaged at any instant (case 2). A third limiting case occurs when the two lengths are comparable, in which the contact line covers the whole width only instantaneously (case 3). Mathematically, the three regimes read:

Case 1: Full face-width engagement

In this case, as mentioned in figure 6, the contact line reaches the start of mesh angle for the hinter face s_h before the front-face tooth finishes mesh e_f. Because the entire face-width is covered, all slices (N_T) participate in the stiffness computation. The temporal evolution of the slice count is assumed linear up to s_h and again linear downwards from e_f, yielding

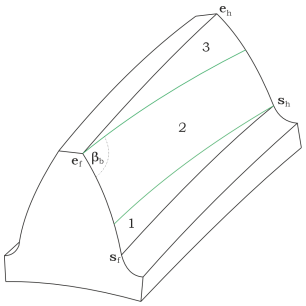


Fig. 6: Contact line in full face-width engagement

$$N(\theta) = \begin{cases} \lfloor\, N_T \, \dfrac{\theta - s_f}{s_h - s_f} \,\rfloor, & s_f \le \theta \le s_h \\ \lfloor\, N_T \, \dfrac{e_h - \theta}{e_h - e_f} \,\rfloor, & e_f \le \theta \le e_h \\ N_T, & \text{otherwise} \end{cases} \tag{43}$$

and the contact-line length is

$$l(\theta) = \begin{cases} \dfrac{(\theta - s_{f,p})\, R_{b,p}}{\sin\beta_b}, & s_{f,p} \le \theta \le s_{h,p} \\ \dfrac{(e_{h,p} - \theta)\, R_{b,p}}{\sin\beta_b}, & e_{f,p} \le \theta \le e_{h,p} \\ \dfrac{(e_{h,p} - s_{f,p})\, R_{b,p}}{\sin\beta_b}, & \text{otherwise} \end{cases} \tag{44}$$

Case 2: Partial face-width engagement

Here the contact line reaches the start of the hinter-face mesh angle s_h after the front-face tooth e_f has finished. Only a fraction of the face-width is engaged, like in figure 7. The maximum number of slices ever covered is

$$N_{\max} = N_T \left\lfloor \frac{(e_{f,p} - s_{f,p})\, R_{b,p}}{W \, \tan\beta_b} \right\rfloor. \tag{45}$$

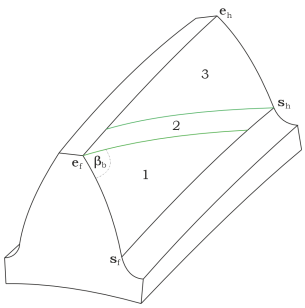


Fig. 7: Contact line in partial face-width engagement

During mesh the slice count follows

$$N(\theta) = \begin{cases} \lfloor\, N_{\max} \, \dfrac{\theta - s_{f,p}}{e_{f,p} - s_{f,p}} \,\rfloor, & s_{f,p} \le \theta \le e_{f,p} \\ \lfloor\, N_{\max} \, \dfrac{e_{h,p} - \theta}{e_{h,p} - s_{h,p}} \,\rfloor, & s_{h,p} \le \theta \le e_{h,p} \\ N_{\max}, & \text{otherwise} \end{cases} \tag{46}$$

and the contact-line length is

$$l(\theta) = \begin{cases} \dfrac{(\theta - s_{f,p})\, R_{b,p}}{\sin \beta_b}, & s_{f,p} \le \theta \le e_{f,p} \\ \dfrac{(e_{h,p} - \theta)\, R_{b,p}}{\sin \beta_b}, & s_{h,p} \le \theta \le e_{h,p} \\ \dfrac{(e_{f,p} - s_{f,p})\, R_{b,p}}{\sin \beta_b}, & \text{otherwise} \end{cases} \tag{47}$$

Case 3: Instantaneous full-Width engagement (Limiting Case)

In this limiting case the contact line reaches the start of the hinter-face mesh angle at exactly the instant the front-face tooth finishes. The entire face-width is covered only for an infinitesimal time as shown in figure 8, but the assumptions about the linear growth of the contact line still hold. The slice count is

$$N(\theta) = \begin{cases} \lfloor N_T \, \dfrac{\theta - s_{f,p}}{e_{f,p} - s_{f,p}} \rfloor, & s_{f,p} \le \theta \le e_{f,p} \\ \lfloor N_T \, \dfrac{e_{h,p} - \theta}{e_{h,p} - s_{h,p}} \rfloor, & s_{h,p} \le \theta \le e_{h,p} \\ N_T, & \text{otherwise} \end{cases} \tag{48}$$

and the contact-line length becomes

$$l(\theta) = \begin{cases} \dfrac{(\theta - s_{f,p})\, R_{b,p}}{\sin \beta_b}, & s_{f,p} \le \theta \le e_{f,p} \\ \dfrac{(e_{h,p} - \theta)\, R_{b,p}}{\sin \beta_b}, & s_{h,p} \le \theta \le e_{h,p} \\ \dfrac{(e_{f,p} - s_{f,p})\, R_{b,p}}{\sin \beta_b}, & \text{otherwise} \end{cases} \tag{49}$$

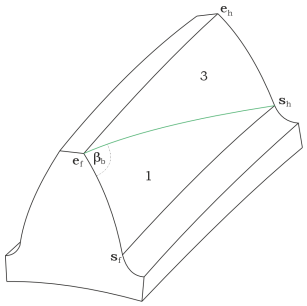


Fig. 8: Contact line in instantaneous face-width engagement

Finally, substituting $N(\theta)$ from Eqs. (43), (46) or (48) into Eq. (18) produces the overall mesh stiffness $k_m(\theta)$ as a function of the roll angle θ.

3 Results

Table 1 summarizes the geometric and material data of the investigated double-helical gear pair. The system is a symmetric pair of double-helical gears with equal normal module, helix angle and face width, both manufactured from steel ($E = 210GPa$, $\nu = 0.30$). The crack geometry employed in this study is an elliptical flaw located in the left row of the driving gear, as illustrated in figure 9. Different crack configurations are analysed, varying in length, depth, and propagation direction, as listed in table 2. The crack may propagate either in a straight-line or a curved trajectory, and its orientation is characterised by a propagation angle measured with respect to the tooth axis.

Parameter	Driving Gear	Driven Gear	Unit
Normal Module	2	2	-
Number of Teeth	40	42	–
Helix Angle	11	11	°
Face Width	20	20	mm
Design Pressure Angle	20	20	°
Elasticity Modulus	210	210	GPa
Poisson Ratio	0.30	0.30	–
Hub Radius	25	25	mm
Groove Width	10	10	mm
Groove Radius	30	30	mm
Applied Torque	100	-	Nm
Speed	4000	-	RPM

Table 1: Parameters of double helical gear system

Each case in table 2 is defined by two numbers that denote the crack length in the right and left directions from the initiation point, a maximum depth, and a set of propagation angles.

Crack length [mm] in right direction	Crack length [mm] in left direction	Crack depth [mm]	Crack propagation angle [°]
5	5	10	1, 10, 20, 45, 60, 88
15	15	15	1, 10, 20, 45, 60, 88
0	5	15	1, 10, 20, 45, 60, 88
0	15	15	1, 10, 20, 45, 60, 88

Table 2: Cases of crack parameter

Figure 10 displays the TVMS curve obtained from the slice-based analytical model for a representative defect scenario in which a crack is centred in the middle of the left row of the driving gear. In this configuration the flaw is an ellipse that extends $10mm$ along the tooth flank ($5mm$ to the left and $5mm$ to the right of

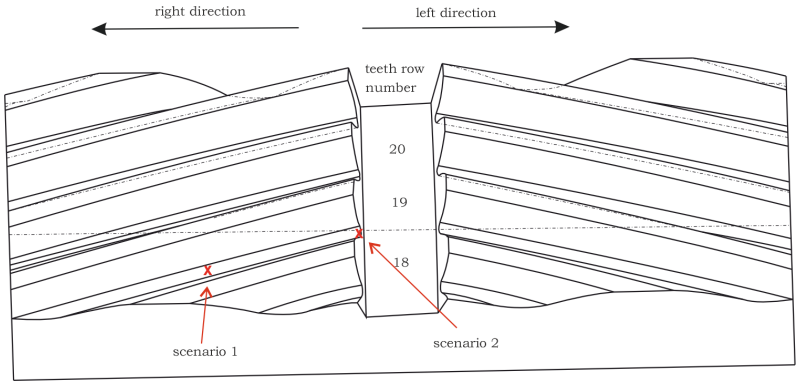


Fig. 9: Schematic illustration of the introduction of a crack into the relevant rows of a double-helical gear

the crack initiation point) and plunges $15mm$ into the gear material. Because the double-helical gear has a face width of $20mm$, this particular crack only occupies a fraction of the tooth width: it does not reach the opposite row of teeth and therefore leaves a healthy, intact section at the outer edge of the tooth.

During one rotation cycle the two rows of teeth on the driving gear exchange contact with the rows on the mating gear. The mesh stiffness is a point-specific measure that evolves as the instantaneous contact point moves along the tooth profile. For the cracked tooth in this case the contact interval is confined to rotation angles between 11.5° and 29.5°. At the start of this interval (just after 11.5°) the mating tooth first touches the outermost, uncracked flank of the defected tooth, whereas at the end of the interval (just before 29.5°) the load centre again lies on this healthy flank as the tooth begins to disengage. Outside the 11.5°–29.5° window the load is carried by neighbouring, intact teeth, and consequently the TVMS of the gear pair returns to its nominal, undamaged level.

Two distinct crack-propagation geometries were examined in this scenario: (i) a straight-line propagation and (ii) a curved-line trajectory. Both paths were simulated for a 1° propagation angle with respect to the tooth axis. The analytical results are somewhat counter-intuitive: during the entire contact interval a modest increase in TVMS is observed for both the straight- and curved-crack models, whereas one would normally expect a reduction of mesh stiffness when a defect is present. This rise in stiffness is only observed for the smallest propagation angle; for all larger angles (10°, 20°, 45°, 60°, 88°) the TVMS curves exhibit the familiar, monotonically decreasing trend that is associated with a damaged tooth. The reason for the anomalous behaviour lies in the fact that the crack does not extend across the entire face width. As the gear turns, the initial and final portions of the contact interval are dominated by load transfer through the intact flank of the tooth, which possesses a higher bending and shear modulus than the cracked section. Consequently, during the beginning and end of the contact phase the effective mesh stiffness is temporarily

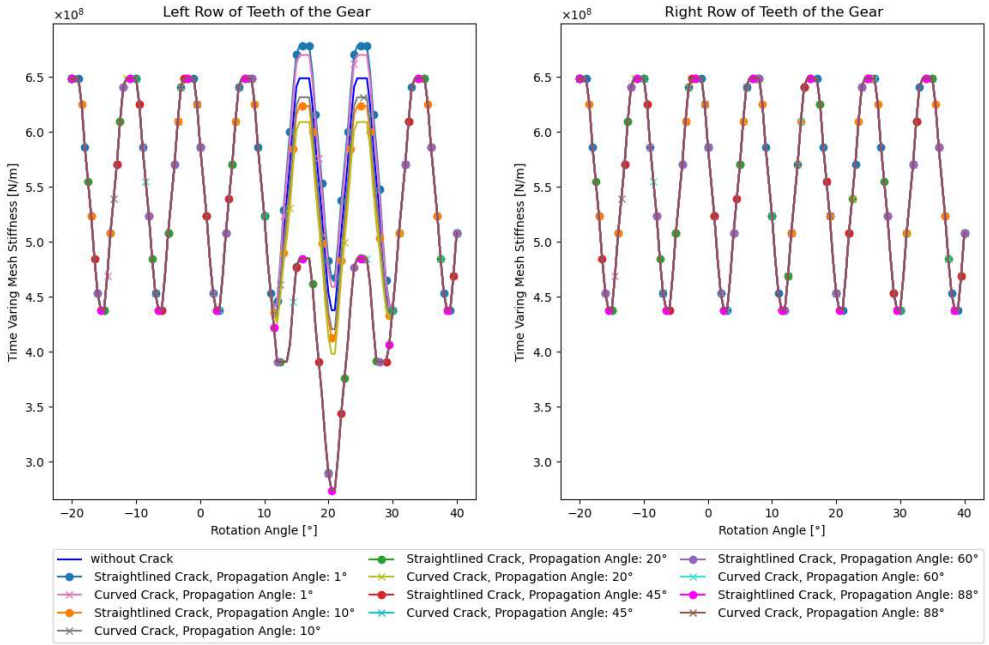


Fig. 10: TVMS trend with crack initiation on the middle of the left row of double helical gear with crack length of $5mm$ in left direction and $5mm$ in right direction and crack depth of $10mm$ and variation of the crack propagation angle

elevated, as the uncracked material still bears the majority of the load. Only once the load centre migrates toward the root of the tooth does the crack become fully engaged, at which point the TVMS declines to its damaged-tooth baseline. The brief stiffness increase therefore reflects a load-path redistribution rather than a genuine stiffening of the cracked material.

When the crack is enlarged so that it spans the full tooth width— $15mm$ in both directions (Figure 11)—the situation changes dramatically. In this fully-spanning defect the entire flank that engages the mating tooth is compromised, and no healthy portion remains to compensate for the loss of compliance. Accordingly the TVMS curves for all examined propagation angles consistently show a decline relative to the undamaged case. The influence of the propagation angle becomes muted once it exceeds 20°: the stiffness curves for 45°, 60°, and 88° collapse onto a common trajectory that differs only marginally from that of the 10° and 20° cases. This collapse indicates that once the crack intercepts the load-bearing line over a sufficiently large arc of the flank, the local stiffness of the tooth becomes almost angle-independent. The most dramatic stiffness drop is observed when the cracked tooth is the only tooth in contact with its mate, because the remaining rows on the gear pair remain intact and can thus carry the bulk of the applied torque. In such a configuration the mesh behaves as if it were loaded by a single, heavily weakened tooth, leading to the

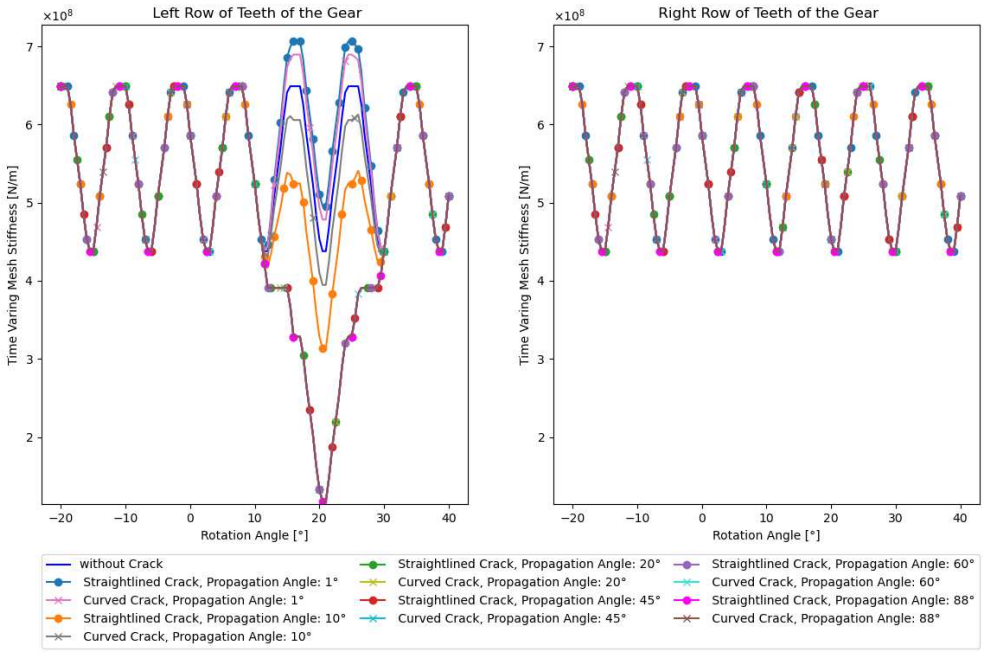


Fig. 11: TVMS trend with crack initiation on the middle of the left row of double helical gear with crack length of $15mm$ in left direction and $15mm$ in right direction and crack depth of $15mm$ and variation of the crack propagation angle

pronounced minimum in TVMS.

The location of the crack initiation point on the tooth also plays a crucial role. Figures 12 and 13 depict two additional cases in which the crack originates at the right edge of the left row of the driving gear. In both scenarios a sizeable healthy portion of the tooth flank remains engaged throughout the contact interval. Consequently, the load path is less severely altered by the defect and the reduction in TVMS is comparatively mild when contrasted with a centrally located crack. Importantly, the curvature of the crack trajectory—straight versus curved—has only a negligible effect on the TVMS for these edge-initiated cases. This insensitivity arises because the uncracked flank of the tooth, which is still in contact with its counterpart, provides a robust load-bearing pathway that dominates the mesh stiffness. Even for very large propagation angles the intact section continues to support most of the load, thereby buffering the effect of the crack.

Collectively, these observations elucidate how the geometry of a crack—its length, depth, propagation angle, and initiation point—dictates the dynamic stiffness of a double-helical gear pair. They also highlight the subtle interplay between tooth contact mechanics and local compliance, explaining why a shallow crack with a very small propagation angle can paradoxically increase the TVMS during the initial and

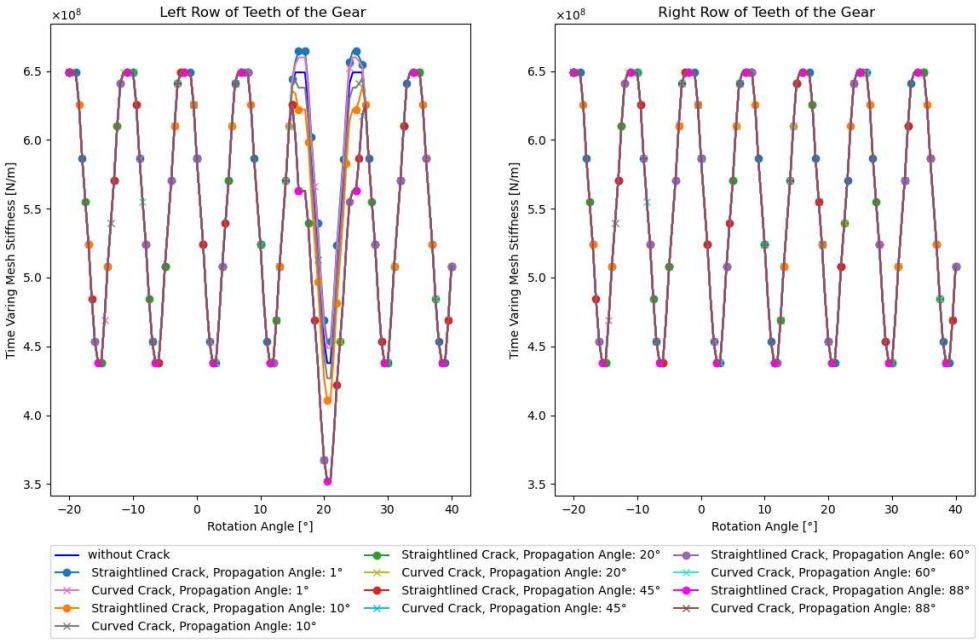


Fig. 12: TVMS trend with crack initiation on the right side of the left row of double helical gear with crack length of $5mm$ in left direction and crack depth of $15mm$ and variation of the crack propagation angle

terminal phases of tooth engagement. Understanding this behaviour is essential for the development of robust damage-tolerant gear designs and for the interpretation of vibration-based health-monitoring data.

Figures 14–16 display the load histories for the three teeth that are immediately adjacent to the defective tooth (teeth 18, 19 and 20) in the left row of the driving gear when the gear pair is uncracked. As the teeth traverse the contact zone, the mesh load first appears on the outermost flank of the tooth and then gradually migrates toward the root. Consequently the force profile on tooth 19 shows a distinct peak in the middle of the contact interval while the forces on teeth 18 and 20 rise and fall symmetrically around this peak. These curves serve as a baseline against which the effect of a crack can be quantified.

The same three teeth are now examined in the presence of a crack that is initiated in the middle of the tooth foot of tooth 19. The crack geometry (figure 9) consists of an elliptical flaw extending $5mm$ to the left and right of the initiation point, with a depth of $5m$ and a propagation angle of 45° (curved trajectory). The force plots for the cracked configuration—shown in figure 17–19—reveal several noteworthy features:

1. Reduction of the load on the defective tooth. The peak force on tooth 19 drops by approximately $0.2N$ compared to the undamaged case. This loss is not merely a

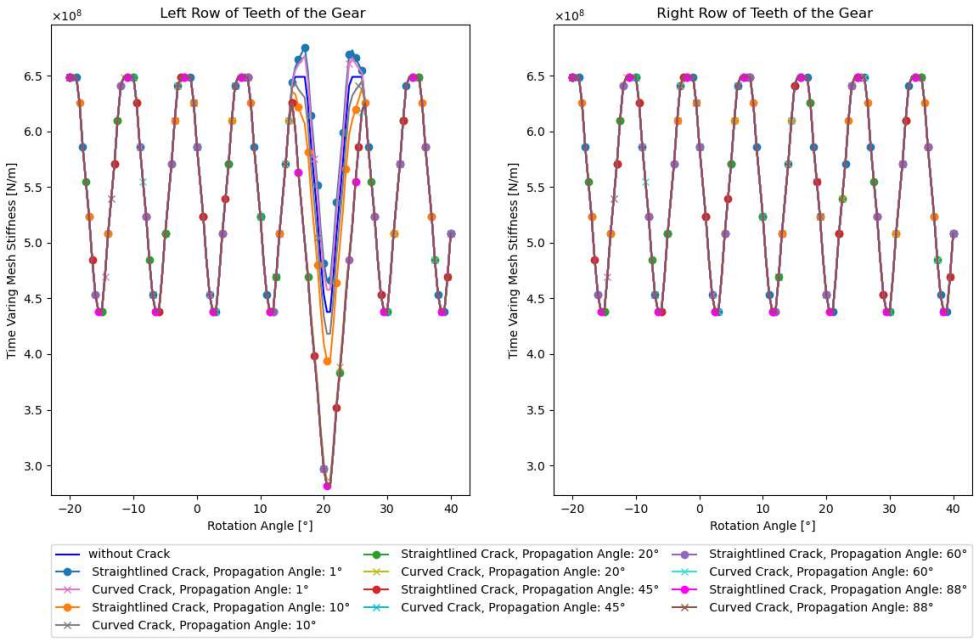


Fig. 13: TVMS trend with crack initiation on the right side of the left row of double helical gear with crack length of $15mm$ in left direction and crack depth of $15mm$ and variation of the crack propagation angle

local effect; about $0.1N$ is transferred to the right tooth 19, which has no crack, while the remaining deficit is distributed between the two neighboring teeth (18 and 20). The redistribution follows the geometry of the mesh: as the load centre moves from the outer flank toward the root, the crack partially shields the tooth from full load, forcing the adjacent teeth to compensate.

2. Load concentration on the preceding tooth (18). In Figure 18 the load on tooth 18 shows a pronounced increase in the early part of the contact interval (rotations $< 10°$). This surge reflects the fact that the defective tooth is still beginning to engage; until the load centre reaches the cracked flank, tooth 18 must carry a larger share of the total load.
3. Load balance in the later part of the contact interval. After 10°, the load on tooth 18 decreases and the load on tooth 20 rises, illustrating the shift of the contact point toward the root of tooth 19. At the very end of the contact interval the load on tooth 19 again drops to near zero, and the remaining force is borne almost entirely by tooth 20, which is now the trailing tooth in the mesh.

The same qualitative behaviour is observed when the crack is extended to fill the entire face width ($15mm$ in both directions, $15mm$ depth, 45° curved propagation, figure 20). In this situation tooth 19 is effectively "invisible" to the mesh at the beginning and at the end of the contact interval (the curves in figure 20 essentially lie on the horizontal axis). All of the load that would normally be transmitted to

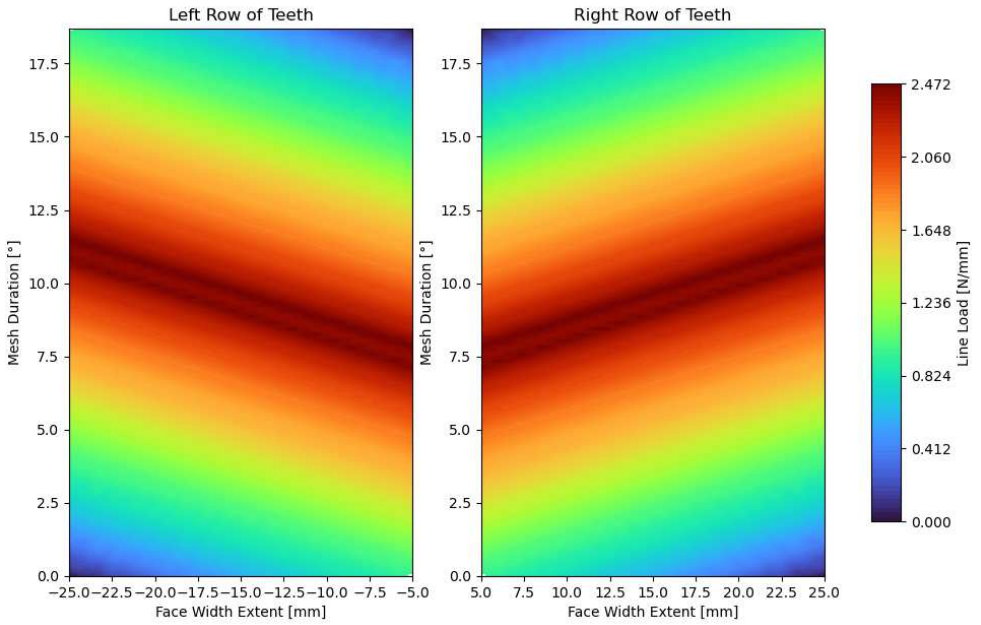


Fig. 14: Force profile on teeth no.19 without crack

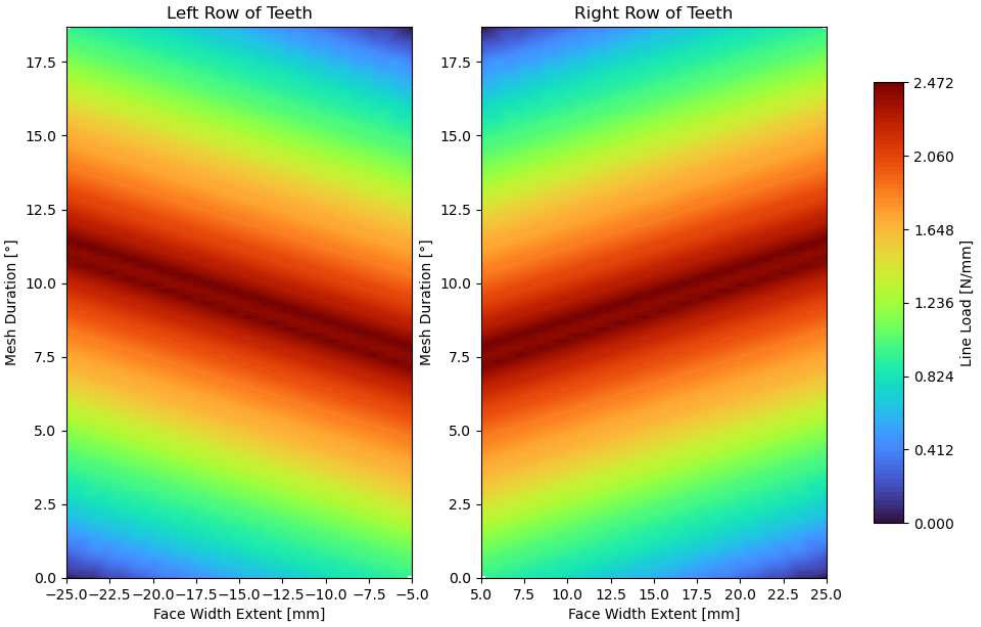


Fig. 15: Force profile on teeth no.18 without crack

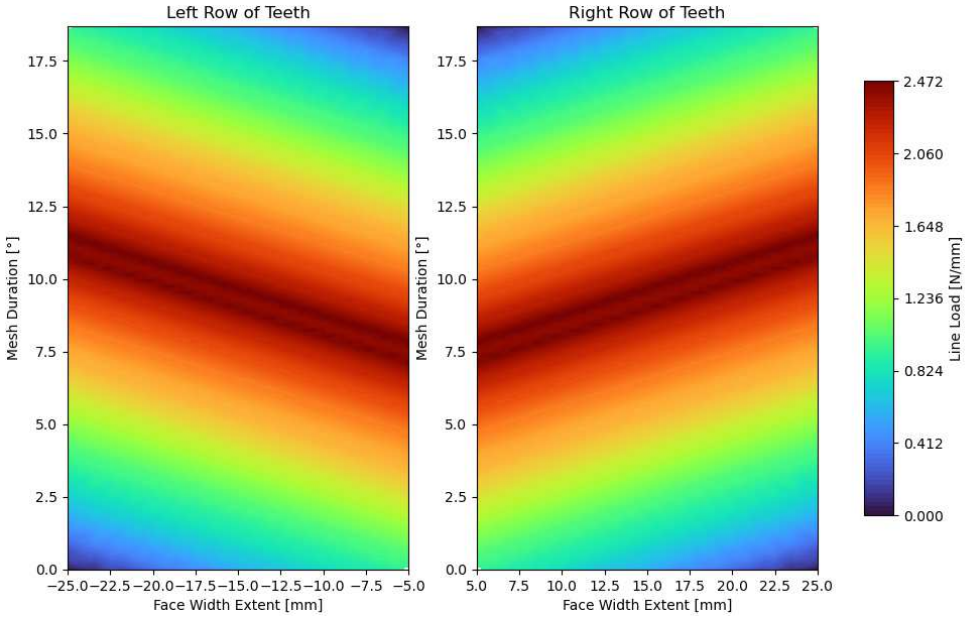


Fig. 16: Force profile on teeth no.20 without crack

tooth 19 is diverted to its neighbours: At the start of the mesh the right-hand side of tooth 19 is in contact, so the load is transferred to tooth 20 (and to tooth 18 to a lesser extent). In the middle of the mesh the load is shared between teeth 18, 19 (very little), and 20, with the balance determined by the precise shape of the contact zone and the curvature of the crack. At the end of the mesh the left flank of tooth 19 would normally engage, but because the crack occupies the entire flank, the load is carried almost exclusively by tooth 18, and the right-hand side tooth 20 becomes the secondary load-bearing member.

These observations underline the high sensitivity of the local force distribution to the geometry of a crack. Even a relatively shallow defect ($5mm$ depth) can alter the load paths by a few hundredths of a newton, while a crack that spans the full face width completely removes a tooth from the load-sharing network, forcing its neighbours to compensate. The curvature and propagation angle influence the timing of these load transfers: a 45° curved crack, for instance, allows the load to "slide" along the flank, whereas a straight crack would abruptly terminate the load path.

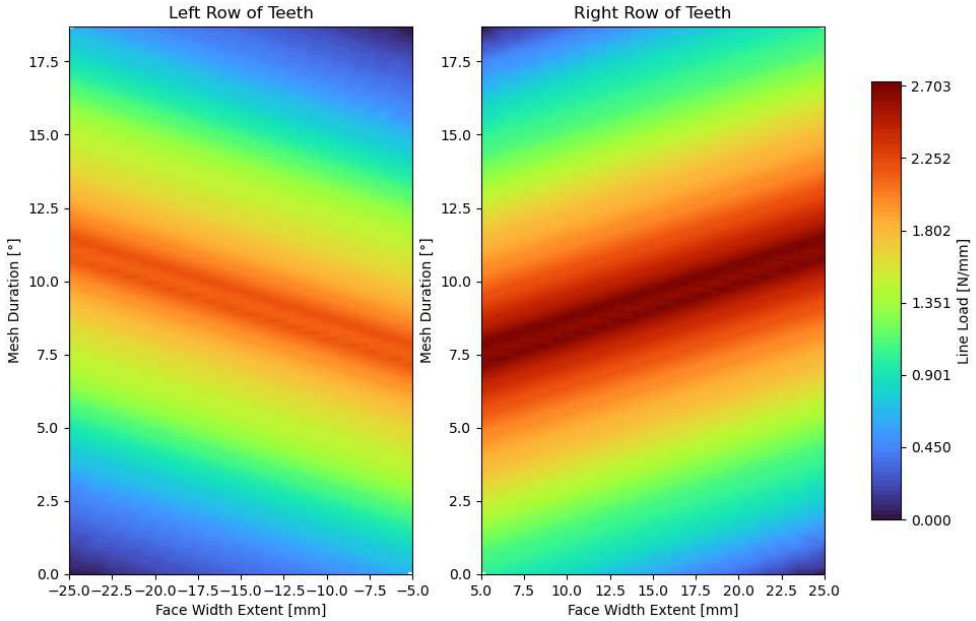


Fig. 17: Force profile on teeth no.19 with crack initiation in the middle of the left row of the gear on the tooth foot of tooth 19 and crack length of $5mm$ in right and left direction, crack depth of $5mm$ and a crack propagation angle of $45°$ for a curved crack

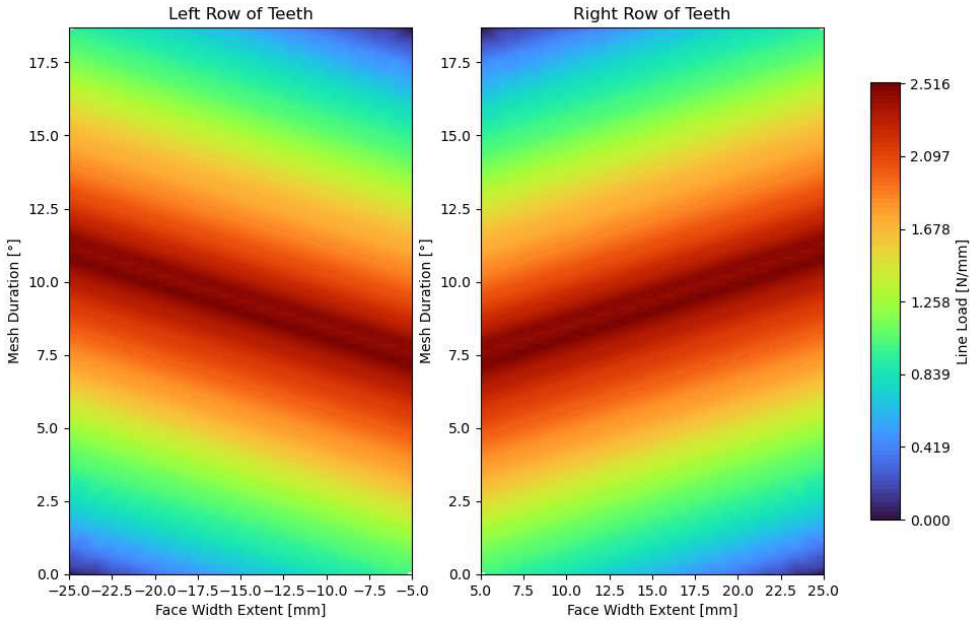


Fig. 18: Force profile on teeth no.18 with crack initiation in the middle of the left row of the gear on the tooth foot of tooth 19 and crack length of $5mm$ in right and left direction, crack depth of $5mm$ and a crack propagation angle of $45°$ for a curved crack

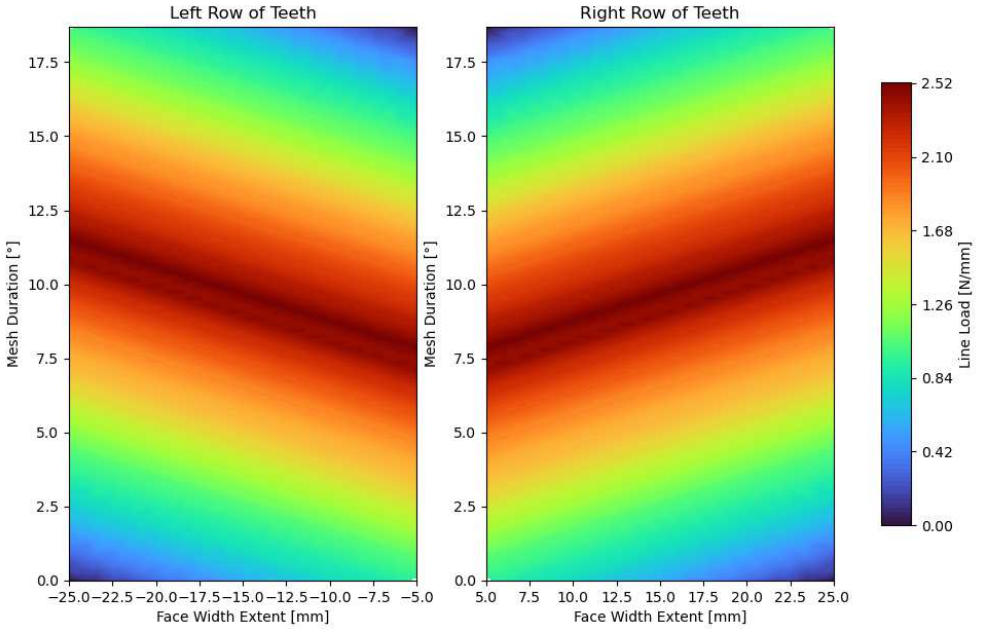


Fig. 19: Force profile on teeth no.20 with crack initiation in the middle of the left row of the gear on the tooth foot of tooth 19 and crack length of $5mm$ in right and left direction, crack depth of $5mm$ and a crack propagation angle of $45°$ for a curved crack

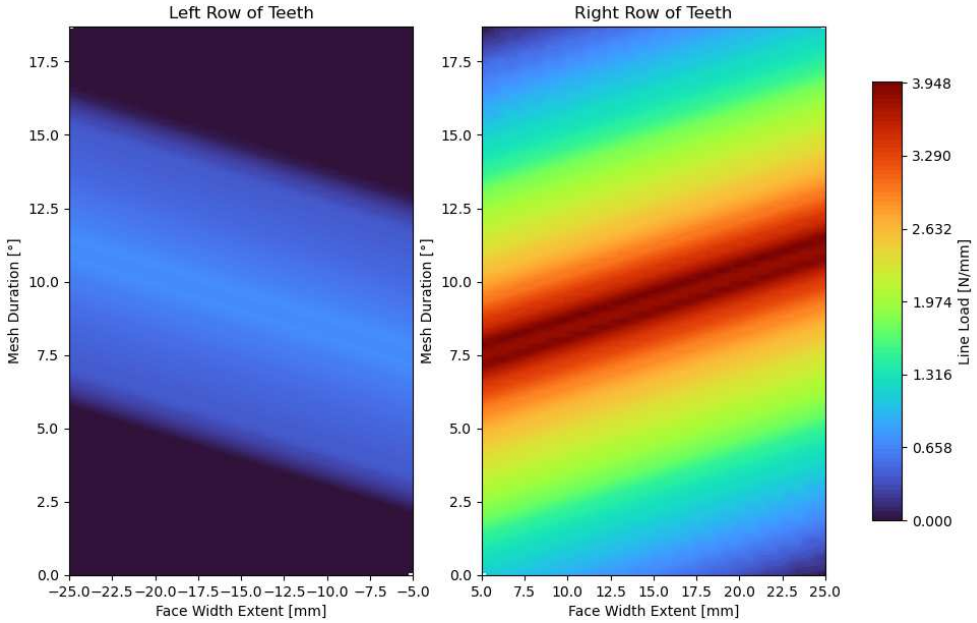


Fig. 20: Force profile on teeth no.19 with crack initiation in the middle of the left row of the gear on the tooth foot of tooth 19 and crack length of $15mm$ in right and left direction, crack depth of $15mm$ and a crack propagation angle of $45°$ for a curved crack

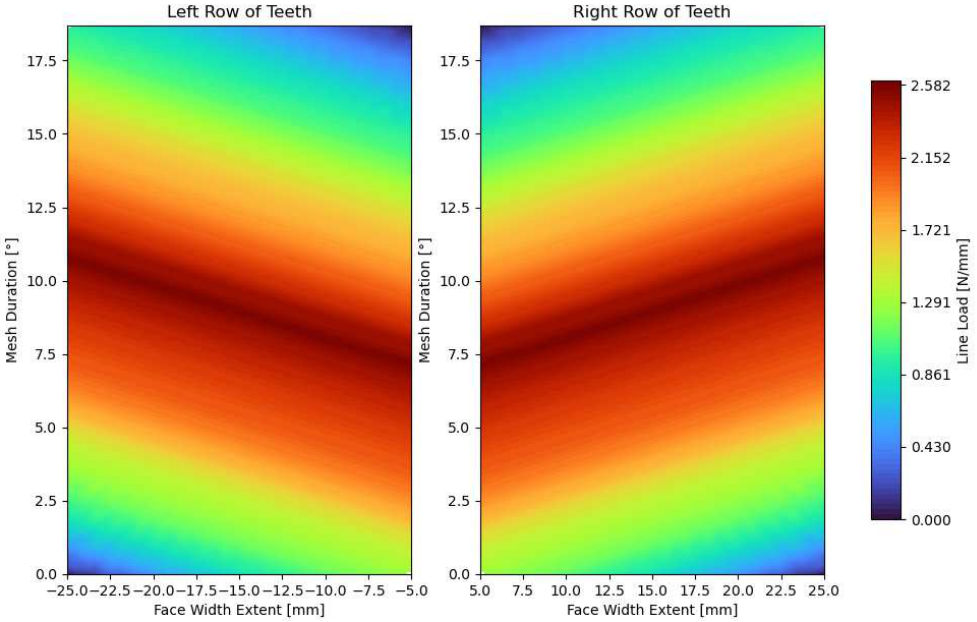


Fig. 21: Force profile on teeth no.18 with crack initiation in the middle of the left row of the gear on the tooth foot of tooth 19 and crack length of $15mm$ in right and left direction, crack depth of $15mm$ and a crack propagation angle of $45°$ for a curved crack

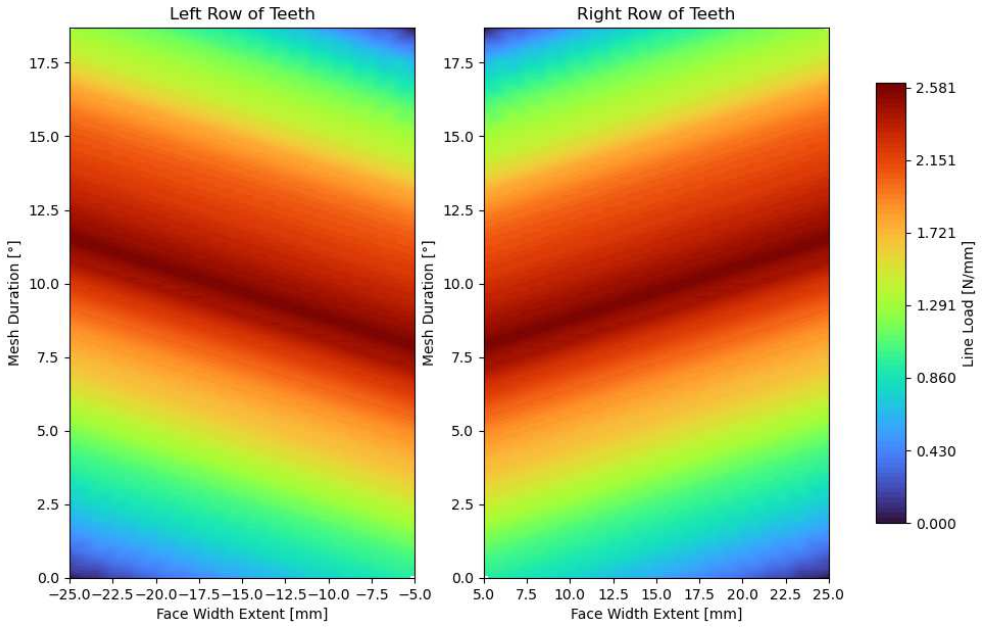


Fig. 22: Force profile on teeth no.20 with crack initiation in the middle of the left row of the gear on the tooth foot of tooth 19 and crack length of $15mm$ in right and left direction, crack depth of $15mm$ and a crack propagation angle of $45°$ for a curved crack

4 Future Work

To set a reliable baseline for the transverse-velocity mesh stiffness (TVMS) framework, the following research directions should be pursued:

1. A comprehensive study of the number of slices in contact, denoted by $N(\theta)$, is essential. The current theory relies on a handful of papers; more visualisation and geometrical insight would strengthen the model. Re-producing the analysis in Section 2 with a rigorously tested mathematical formulation would provide a valuable benchmark.
2. The mesh-stiffness behaviour of double-helical gears warrants further scrutiny. The model employed in this report is adapted from Yang *etal.*[32], but its assumptions and derivations should be examined in greater depth.
3. Acquisition of high-quality experimental data on the forces acting on gear teeth (using calibrated testing rigs) would enable researchers to reverse-engineer the stiffness calculation and establish a robust, top-down benchmark for the community.

In short, substantial improvements to the TVMS methodology are necessary. This report's goal extends beyond a mere force evaluation; it is intended to streamline literature discovery and model development for those interested in advancing gear-stiffness research.

5 Declaration

Funding

The project on which this report is based was funded by the Federal Ministry for Economic Affairs and Energy under grant reference number 20T2101B. The author is responsible for the content of this publication. The authors also express their gratitude to Rolls-Royce Deutschland Ltd & Co KG for the collaboration and support in this project.

Competing interests

The authors have no competing interests to declare that are relevant to the content of this article.

Author Contribution

S.-M.R. (Sophie-Maria Rauscher) supervised the research and acted as the corresponding author. S.-M.R. and A.T. (Aryan Thosar) performed the simulations, generated the results and wrote the main manuscript. A.T. and B.N. (Behara Neha) developed the theoretical framework of this work.

Data Availablility

The datasets generated during and/or analysed during the current study are not publicly available but are available from the corresponding author on reasonable request.

References

[1] Yang, L., Zou, D., Sun, X., Wang, L., Shao, Y., Gu, F., Ball, A., Mba, D.: Dynamic modelling and analysis of cracked gear system with tip relief based on proposed variable-angle deformation energy integration method. Nonlinear Dynamics **111**(5), 4141–4172 (2022) https://doi.org/10.1007/s11071-022-08077-z

[2] Ma, H., Song, R., Pang, X., Wen, B.: Time-varying mesh stiffness calculation of cracked spur gears. Engineering Failure Analysis **44**, 179–194 (2014) https://doi.org/10.1016/j.engfailanal.2014.05.018

[3] Cao, Z., Chen, Z., Jiang, H.: Nonlinear dynamics of a spur gear pair with force-dependent mesh stiffness. Nonlinear Dynamics **99**(2), 1227–1241 (2019) https://doi.org/10.1007/s11071-019-05348-0

[4] Feng, M., Ma, H., Li, Z., Wang, Q., Wen, B.: An improved analytical method for calculating time-varying mesh stiffness of helical gears. Meccanica **53**(4–5), 1131–1145 (2017) https://doi.org/10.1007/s11012-017-0746-6

[5] Gu, X., Velex, P., Sainsot, P., Bruyère, J.: Analytical investigations on the mesh stiffness function of solid spur and helical gears. Journal of Mechanical Design **137**(6) (2015) https://doi.org/10.1115/1.4030272

[6] Liu, L., Ding, Y.F., Wu, L.Y., Liu, G.: Effects of contact ratios on mesh stiffness of helical gears for lower noise design, pp. 320–329. Elsevier, ??? (2014). https://doi.org/10.1533/9781782421955.320

[7] Choe, T.-C., Ri, C.-N., Jo, M.-J., Ri, M.-C.: Research on the engagement process and contact line of involute helical gears. Mechanism and Machine Theory **171**, 104778 (2022) https://doi.org/10.1016/j.mechmachtheory.2022.104778

[8] Marafona, J.D.M., Marques, P.M.T., Martins, R.C., Seabra, J.H.O.: Mesh stiffness models for cylindrical gears: A detailed review. Mechanism and Machine Theory **166**, 104472 (2021) https://doi.org/10.1016/j.mechmachtheory.2021.104472

[9] Zheng, X., Luo, W., Hu, Y., He, Z., Wang, S.: Analytical approach to mesh stiffness modeling of high-speed spur gears. International Journal of Mechanical Sciences **224**, 107318 (2022) https://doi.org/10.1016/j.ijmecsci.2022.107318

[10] Yang, Y., Cao, L., Li, H., Dai, Y.: Nonlinear dynamic response of a spur gear pair based on the modeling of periodic mesh stiffness and static transmission error. Applied Mathematical Modelling **72**, 444–469 (2019) https://doi.org/10.1016/j.apm.2019.03.026

[11] Jiang, H., Shao, Y.: Dynamic analysis of a multi-mesh gear system with mesh stiffness variation. In: Volume 5: 25th International Conference on Design Theory and Methodology; ASME 2013 Power Transmission and Gearing Conference.

IDETC-CIE2013. American Society of Mechanical Engineers, ??? (2013). https://doi.org/10.1115/detc2013-12750

[12] Chang, L., Liu, G., Wu, L.: A robust model for determining the mesh stiffness of cylindrical gears. Mechanism and Machine Theory **87**, 93–114 (2015) https://doi.org/10.1016/j.mechmachtheory.2014.11.019

[13] Kahraman, A., Ozguven, H.N., Houser, D.R., Zakrajsek, J.J.: Dynamic analysis of geared rotors by finite elements. Journal of Mechanical Design **114**(3), 507–514 (1992) https://doi.org/10.1115/1.2926579

[14] Chen, Z., Shao, Y.: Mesh stiffness of an internal spur gear pair with ring gear rim deformation. Mechanism and Machine Theory **69**, 1–12 (2013) https://doi.org/10.1016/j.mechmachtheory.2013.04.017

[15] Patel, A., Shakya, P.: Spur gear crack modelling and analysis under variable speed conditions using variational mode decomposition. Mechanism and Machine Theory **164**, 104357 (2021) https://doi.org/10.1016/j.mechmachtheory.2021.104357

[16] Tian, X.: Dynamic simulation for system response of gearbox including localized gear faults. PhD thesis, University of Alberta (2004). https://doi.org/10.7939/R3-05S3-BY17

[17] Wu, S., Zuo, M.J., Parey, A.: Simulation of spur gear dynamics and estimation of fault growth. Journal of Sound and Vibration **317**(3–5), 608–624 (2008) https://doi.org/10.1016/j.jsv.2008.03.038

[18] El Yousfi, B., Soualhi, A., Medjaher, K., Guillet, F.: New approach for gear mesh stiffness evaluation of spur gears with surface defects. Engineering Failure Analysis **116**, 104740 (2020) https://doi.org/10.1016/j.engfailanal.2020.104740

[19] Pandya, Y., Parey, A.: Simulation of crack propagation in spur gear tooth for different gear parameter and its influence on mesh stiffness. Engineering Failure Analysis **30**, 124–137 (2013) https://doi.org/10.1016/j.engfailanal.2013.01.011

[20] Zhou, X., Shao, Y., Lei, Y., Zuo, M.: Time-varying meshing stiffness calculation and vibration analysis for a 16dof dynamic model with linear crack growth in a pinion. Journal of Vibration and Acoustics **134**(1) (2011) https://doi.org/10.1115/1.4004683

[21] Shao, R., Jia, P., Dong, F.: Dynamic characteristics of cracked gear and three-dimensional crack propagation analysis. Proceedings of the Institution of Mechanical Engineers, Part C: Journal of Mechanical Engineering Science **227**(6), 1341–1361 (2012) https://doi.org/10.1177/0954406212461326

[22] Yu, W., Shao, Y., Mechefske, C.K.: The effects of spur gear tooth spatial crack

propagation on gear mesh stiffness. Engineering Failure Analysis **54**, 103–119 (2015) https://doi.org/10.1016/j.engfailanal.2015.04.013

[23] Jiang, H., Liu, F.: Analytical models of mesh stiffness for cracked spur gears considering gear body deflection and dynamic simulation. Meccanica **54**(11–12), 1889–1909 (2019) https://doi.org/10.1007/s11012-019-01053-9

[24] Zouari, S., Maatar, M., Fakhfakh, T., Haddar, M.: Three-dimensional analyses by finite element method of a spur gear: Effect of cracks in the teeth foot on the mesh stiffness. Journal of Failure Analysis and Prevention **7**(6), 475–481 (2007) https://doi.org/10.1007/s11668-007-9078-5

[25] Liang, X., Zuo, M.J., Pandey, M.: Analytically evaluating the influence of crack on the mesh stiffness of a planetary gear set. Mechanism and Machine Theory **76**, 20–38 (2014) https://doi.org/10.1016/j.mechmachtheory.2014.02.001

[26] Saxena, A., Chouksey, M., Parey, A.: Effect of mesh stiffness of healthy and cracked gear tooth on modal and frequency response characteristics of geared rotor system. Mechanism and Machine Theory **107**, 261–273 (2017) https://doi.org/10.1016/j.mechmachtheory.2016.10.006

[27] Lewicki, D.G., Ballarini, R.: Rim thickness effects on gear crack propagation life. International Journal of Fracture **87**(1), 59–86 (1997) https://doi.org/10.1023/a:1007368801853

[28] Zouari, S., Maatar, M., Fakhfakh, T., Haddar, M.: Following spur gear crack propagation in the tooth foot by finite element method. Journal of Failure Analysis and Prevention **10**(6), 531–539 (2010) https://doi.org/10.1007/s11668-010-9395-y

[29] Chen, Z., Shao, Y.: Dynamic simulation of spur gear with tooth root crack propagating along tooth width and crack depth. Engineering Failure Analysis **18**(8), 2149–2164 (2011) https://doi.org/10.1016/j.engfailanal.2011.07.006

[30] Chen, K., Huangfu, Y., Ma, H., Xu, Z., Li, X., Wen, B.: Calculation of mesh stiffness of spur gears considering complex foundation types and crack propagation paths. Mechanical Systems and Signal Processing **130**, 273–292 (2019) https://doi.org/10.1016/j.ymssp.2019.05.014

[31] Wu, X., Luo, Y., Li, Q., Shi, J.: A revised method to calculate time-varying mesh stiffness of helical gear. MATEC Web of Conferences **355**, 01005 (2022) https://doi.org/10.1051/matecconf/202235501005

[32] Yang, J., Lin, T., He, Z., Chen, M.: Novel calculation method for dynamic excitation of modified double-helical gear transmission. Mechanism and Machine Theory **167**, 104467 https://doi.org/10.1016/j.mechmachtheory.2021.104467

[33] Wang, Q., Zhao, B., Fu, Y., Kong, X., Ma, H.: An improved time-varying mesh

stiffness model for helical gear pairs considering axial mesh force component. Mechanical Systems and Signal Processing **106**, 413–429 (2018) https://doi.org/10.1016/j.ymssp.2018.01.012

[34] Luo, Y., Baddour, N., Liang, M.: Effects of gear center distance variation on time varying mesh stiffness of a spur gear pair. Engineering Failure Analysis **75**, 37–53 (2017) https://doi.org/10.1016/j.engfailanal.2017.01.015

[35] Sainsot and, P., Velex, P., Duverger, O.: Contribution of gear body to tooth deflections—a new bidimensional analytical formula. Journal of Mechanical Design **126**(4), 748–752 (2004) https://doi.org/10.1115/1.1758252